Towards a real-time fully-coherent all-sky search for gravitational waves from compact binary coalescences using particle swarm optimization

Marc E. Normandin
Dept. of Biology, University of Texas San Antonio, One UTSA Circle, San Antonio, TX 78249

Soumya D. Mohanty
Dept. of Physics and Astronomy, University of Texas Rio Grande Valley, One West University Blvd., Brownsville, Texas 78520

arXiv:2002.02150v3 [astro-ph.IM] 20 Mar 2020

While a fully-coherent all-sky search is known to be optimal for detecting gravitational wave signals from compact binary coalescences, its high computational cost has limited current searches to less sensitive coincidence-based schemes. Following up on previous work that has demonstrated the effectiveness of Particle Swarm Optimization in reducing the computational cost of this search, we present an implementation that achieves near real-time computational speed. This is achieved by combining the search efficiency of PSO with a significantly revised and optimized numerical implementation of the underlying mathematical formalism along with additional multi-threaded parallelization layers in a distributed computing framework. For a network of four second-generation detectors with 60 min data from each, the runtime of the implementation presented here ranges between ≈ 1.4 to ≈ 0.5 times the data duration for network signal-to-noise ratios (SNRs) of $\gtrsim 10$ and $\gtrsim 12$, respectively. The reduced runtimes are obtained with small to negligible losses in detection sensitivity: for a false alarm rate of $\simeq 1$ event per year in Gaussian stationary noise, the loss in detection probability is $\leq 5\%$ and $\leq 2\%$ for SNRs of 10 and 12, respectively. Using the fast implementation, we are able to quantify frequentist errors in parameter estimation for signals in the double neutron star mass range using a large number of simulated data realizations. A clear dependence of parameter estimation errors and detection sensitivity on the condition number of the network antenna pattern matrix is revealed. Combined with previous work, this paper securely establishes the effectiveness of PSO-based fully-coherent all-sky search across the entire binary inspiral mass range that is relevant to ground-based detectors.

I. INTRODUCTION

A network of spatially well-separated gravitational wave (GW) detectors is a critical requirement for GW astronomy. A detector network is essential for estimating the waveforms of the two polarizations of a GW signal and for localizing its source on the sky. Optimally combining the data from a detector network leads to improved GW search sensitivity.

Starting with GW150914 [1], a binary black hole inspiral and merger detected by the two-detector LIGO [2] network, the LIGO-only and the LIGO-Virgo network collected 11 confirmed compact binary coalescence (CBC) events over two observing runs [3], O1 and O2. The addition of Virgo [4] to the network played a particularly important role in shrinking the localization error for GW170817 [5], the coalescence of a double neutron star binary, leading to the spectacular discovery of an electromagnetic counterpart [6]. The LIGO-Virgo network is slated to be joined by the Japanese KAGRA [7] detector sometime during the ongoing (O3) observing run. In the near future, the planned worldwide network of five second-generation GW detectors will be completed with the construction and commissioning of LIGO-India [8].

It is well-known that the optimal methods for the detection and estimation of CBC signals with network data [9] are the intimately related Maximum Likelihood Estimation (MLE) [10] and Generalized Likelihood Ratio Test (GLRT) [11], respectively. Both MLE and GLRT, conflated under the commonly used term fully-coherent all-sky search (FCAS) [12], require the global optimization of the joint likelihood function of data from a detector network over the full parameter space of CBC signals, which includes the two sky angles, the masses of the binary components, and the components of their spins.

While optimal, the computational cost of FCAS is daunting if the global optimization is carried out over a regular grid in parameter space. The addition of a grid in the sky angles is estimated to increase the number of grid points by a factor of $O(10^3)$ over that for a single detector search [12]. This computational bottleneck has prevented an always-on FCAS search from being used on all of the data from a detector network. Instead, all search methods at present use a semi-coherent scheme in which the data from each detector is first searched separately and only those events that pass a pair-wise coincidence test [13] are followed up by FCAS search. The inability to deploy FCAS search on all data has been estimated to result in a 25% loss in the detection volume for the first-generation LIGO-Virgo network [12].

Even with the drastically reduced live-time of the FCAS step in semi-coherent searches, grid-based optimization of the network likelihood for parameter estimation remains computationally infeasible. Instead, a Markov Chain Monte Carlo (MCMC) based stochastic optimization approach [14] is used to estimate the parameters of candidate events. However, MCMC based methods are themselves computationally expensive and

slow, requiring another method called BAYESTAR [15] that approximates the full MCMC to deliver rapid sky localizations for electromagnetic follow ups. The speed of this method derives from using estimated values of parameters, other than the sky location, from the coincidence step. As such, it cannot serve as an FCAS search method.

Besides enhanced sensitivity, overcoming the computational barrier of an always-on FCAS search promises other potential advantages over semi-coherent searches. One is a simpler implementation that eliminates much of the empirical tuning based on ad hoc criteria that is involved in semi-coherent searches, such as the tuning of per-detector detection thresholds and coincidence window size. Another is that network analysis allows new kinds of vetoes [16] to be developed for non-astrophysical signals ("glitches"), further improving the sensitivity of an FCAS search.

It has been demonstrated in several studies by now that Particle Swarm Optimization (PSO) [17–20] offers a promising path forward in drastically reducing the computational cost of CBC searches. The first application of PSO to a GW data analysis problem in Ref. [21] demonstrated its effectiveness for a single-detector CBC search. The application of PSO to FCAS search was proposed in Ref. [22] (WM) and, for a network of first-generation detectors, showed a 10-fold reduction in the number of likelihood evaluations compared to grid-based optimization. This prompted further developments in Ref. [23] (NMW), where it was shown that the reduced computational burden of a PSO-based FCAS search also holds for data from a second-generation detector network. In addition, a faster code was developed and improved convergence to the global maximum was obtained by changing the variant of PSO used in the search. An application of PSO to semi-coherent search itself [24] has shown a large reduction in computational costs, further bolstering the evidence for its effectiveness.

In this paper, we present the next major step in the evolution of the PSO-based FCAS search: an optimized numerical implementation of the mathematical formalism combined with a multi-layered parallelized implementation that brings us to the doorstep of a real-time FCAS search. (By real-time, we mean a search that analyzes T sec of data in T sec of wall-clock time.) The latest version of the code, called BINARIES (Binary Inspiral Network Analysis Rapid Implementation Enabled by Swarm intelligence), can analyze $\approx$ 60 min of data in $\approx$ 80 min of wall-clock time for a target four-detector network signal-to-noise ratio (SNR) of 10.0. The code becomes significantly faster than real-time if the target is relaxed to SNR $\gtrsim$ 12 since the number of PSO iterations needed for the search are reduced considerably.

The efficient implementation of the mathematical formalism of FCAS search presented in this paper differs significantly from the one used in both WM and NMW. The parallelization layers are increased from two in NMW to three here through major changes, such as shifting to a multi-threaded numerical algorithms library. Together, these two developments make BINARIES ≈ 22 times faster than the code used in NMW on the same computing hardware.

Using BINARIES, we are able to obtain, for the first time, Frequentist error estimates for sky localization and chirp time parameters for the challenging case of a representative low mass ($1.5M_\odot$,$1.5M_\odot$) binary inspiral signal embedded in 60 min of data. This overcomes the limitations of WM and NMW to shorter signals and establishes the applicability of PSO-based FCAS search across the entire mass range of binary inspirals relevant to ground-based detectors. Using direct numerical estimation allows a more realistic assessment of parameter estimation errors than analytic estimates based on the Cramer-Rao Lower Bound (CRLB) [10] that is only attained asymptotically at high SNR. Further changes implemented in the present paper include the use of detector-specific design sensitivity curves instead of the same, advanced LIGO, one for all. The resulting error estimates are, therefore, relevant to the actual worldwide detector network.

The rest of the paper is organized as follows. Sec. II provides a review of the FCAS search formalism, the noise and signal models used in this paper, and the changes made to the numerical implementation of the formalism. Sec. III discusses PSO and the tuning process used to optimize its performance. The runtime analysis of BINARIES is examined in Sec. IV. Results on the detection and estimation performance of BINARIES on simulated data are presented in Sec. V. We conclude with a discussion of the results and pointers to future investigations in Sec. VI.

II. FULLY-COHERENT ALL-SKY SEARCH

Much of the mathematical formalism for the fully-coherent all-sky search remains the same as in WM and NMW that, in turn, closely follow [9]. In this paper, we focus more on those aspects of the formalism that were modified to improve the efficiency of its numerical implementation.

A T sec long segment of data from the ith detector in a network of D detectors is denoted by $x^i(t)$. Under the null (H_0) and alternative (H_1) hypotheses,

$$x^i(t) = n^i(t) \,, \tag{1}$$

and

$$x^i(t) = h^i(t) + n^i(t) \,, \tag{2}$$

respectively, where $n^i(t)$ is a noise realization and $h^i(t)$ is the strain response of the detector to an incident GW signal.

For a source located at azimuthal angle α and polar angle δ in the Earth Centered Earth Fixed Frame

(ECEF) [25], the detector responses are given by,

$$\begin{pmatrix} h^1(t+\Delta^1(\alpha,\delta)) \\ h^2(t+\Delta^2(\alpha,\delta)) \\ \vdots \\ h^D(t+\Delta^D(\alpha,\delta)) \end{pmatrix} = \mathbf{F}(\alpha,\delta,\psi) \begin{pmatrix} h_+(t) \\ h_\times(t) \end{pmatrix} , \quad (3)$$

where the i^{th} row of the antenna pattern matrix $\mathbf{F}(\alpha,\delta,\psi)$ contains the antenna pattern functions $(F^i_+(\alpha,\delta,\psi),\ F^i_\times(\alpha,\delta,\psi))$ of the i^{th} detector, $h_+(t)$ and $h_\times(t)$ are the TT gauge polarization components of the GW plane wave incident on the origin of the ECEF, and $\Delta^i(\alpha,\delta)$ is the time delay between the plane wave hitting the ECEF origin and the i^{th} detector. The polarization angle ψ gives the orientation of the wave frame axes with respect to the fiducial basis formed by $-\widehat{\alpha}$ and $\widehat{\delta}$ in the plane orthogonal to the wave propagation direction.

A. Noise model

In common with theoretical studies of detection and estimation performance of CBC search algorithms, we assume that $n^i(t)$ is the realization of a stationary zero-mean Gaussian process with one-sided power spectral density (PSD) $S^i_n(f)$ at Fourier frequency f. Further, $n^i(t)$ and $n^j(t)$, $i \neq j$, are assumed to be realizations of statistically independent stochastic processes. Figure 1 shows the PSDs used in this paper in the form of strain sensitivity curves ($\sqrt{S^i_n(f)}$). These correspond to the design sensitivities of the two aLIGO detectors at Hanford (H) and Livingston (L), advanced Virgo (V), and KAGRA (K).

Several high power narrowband noise features ("lines") are present in the design sensitivity of KAGRA. Due to their adverse impact on the dynamic range of data and the associated numerical errors in its processing, the generation of simulated KAGRA noise must use a PSD that models the removal of these features. However, without considering a specific line removal or whitening method, it is not possible to deduce how much of the bandwidth associated with each line should be notched or set to zero. In this paper, we follow the simple approach of interpolating the noise floor across each line (leaving behind a slight bump). Since the signal power in the corresponding bands is not suppressed to the same amount as the lines, we incur an overestimate of parameter estimation accuracy. We leave it to future work to revisit this issue more carefully once the characteristics of real KAGRA noise and specific line removal methods have been established. It should be noted that lines are present in real data from all interferometic GW detectors and they are mitigated in the data conditioning step that precedes any analysis of real data. The line mitigation step in data conditioning for an FCAS search can be the same as the one used in a semi-coherent search.

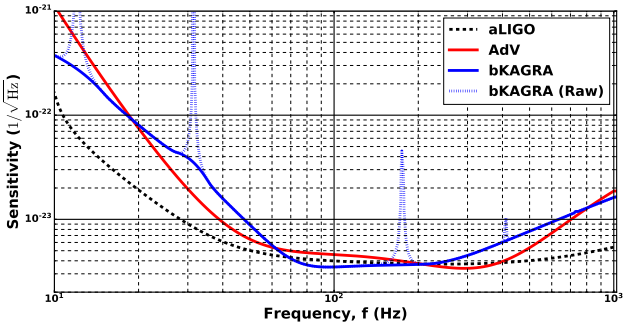


FIG. 1. Strain sensitivity curves used in this paper for aLIGO (Hanford and Livingston), advanced Virgo, and KAGRA. The curves are labeled, respectively, as aLIGO, AdV, and bKAGRA. The aLIGO curve is obtained from [26]. The bKAGRA interpolates across the lines in the actual curve [27] labeled as bKAGRA (Raw) in the figure. The AdV curve is obtained from [28].

B. Signal waveform

The polarization waveforms used in this paper are obtained from the restricted 2-PN formalism [29] for a circularized binary with non-spinning components. In this paper, we only need to show the waveforms schematically, with more detailed expressions available in, for example, WM. Under the stationary phase approximation, the waveforms in the Fourier domain are

$$\widetilde{h}_+(f) = A_+ f^{-7/6} \exp[-i\Psi(f)] , \quad (4)$$

$$\widetilde{h}_\times(f) = A_\times f^{-7/6} \exp[-i(\Psi(f)+\pi/2)] , \quad (5)$$

$$\Psi(f) = 2\pi f t_c - \phi_c - \pi/4 + \psi(f) \quad (6)$$

where $\psi(f)$ belongs to a two parameter family of smooth functions. The parameters depend on the masses, m_1 and m_2, of the binary components but instead of using them directly, it is more convenient to use the chirp time parameters τ_0 and $\tau_{1.5}$

$$\tau_0 = \frac{5}{256\pi} f_*^{-1} \left(\frac{GM}{c^3}\pi f_*\right)^{-5/3} \eta^{-1} , \quad (7)$$

$$\tau_{1.5} = \frac{1}{8} f_*^{-1} \left(\frac{GM}{c^3}\pi f_*\right)^{-2/3} \eta^{-1} , \quad (8)$$

$$M = m_1 + m_2 , \quad \mu = \frac{m_1 m_2}{M} , \quad \eta = \frac{\mu}{M} , \quad (9)$$

where f_* denotes the low-frequency cutoff of a high pass filter that must be applied to GW detector data before commencing any search in order to suppress the steep rise in $S^i_n(f)$ due to seismic noise. The effect of the high pass filter is taken into account by setting $\widetilde{h}_{+,\times}(f) = 0$ for $f \leq f_*$. While f_* is arguably detector-specific, we adopt a common value of $f_* = 10$ Hz in this paper for all second generation detectors.

The other parameters defining the waveforms are the overall amplitudes $A_{+,\times}$, which depend purely on the distance to the binary and its orientation relative to the

line of sight; the time, t_c, between the instantaneous frequency of the inspiral signal crossing f_* and the plunge at the last stable orbit that ends the inpiral; the instantaneous phase, ϕ_c, of the waveforms at t_c.

Besides the low-frequency cutoff, f_*, all waveforms also have a high frequency cutoff caused by the plunge. While this cutoff depends on the mass parameters of the system, the amount of time a low mass system spends near plunge contributes very few cycles to the waveform relative to the inspiral phase, allowing the waveform model to use a generic high frequency cutoff. This is set to 1000 Hz for the waveforms considered in this paper.

C. Detection and estimation

For the noise model used in this paper, the log-likelihood ratio for a D detector network is given by,

$$\lambda^{(D)} = \sum_{i=1}^{D} \left[\langle x^i | h^i \rangle^i - \frac{1}{2} \langle h^i | h^i \rangle^i \right] , \tag{10}$$

$$h^i = \sum_{k=1}^{4} A_k h_k^i (t - \Delta^i) , \tag{11}$$

$$\langle\, p \mid q \,\rangle^i = 4\, \mathrm{Re} \int_0^\infty df\, \frac{\widetilde{p}(f) \widetilde{q}^*(f)}{S_n^i(f)} . \tag{12}$$

Here, we have used the fact that $A_{+,\times}$, ψ, and ϕ_c can be reparametrized as amplitudes, A_k, of the so-called template waveforms

$$\begin{aligned} h_1^i(t) &= U_+^i h_c(t), \quad h_2^i(t) = U_\times^i h_c(t), \\ h_3^i(t) &= U_+^i h_s(t), \quad h_4^i(t) = U_\times^i h_s(t), \end{aligned} \tag{13}$$

where $U_a^i = F_a^i(\alpha, \delta, 0)$, $a = +, \times$, and $\widetilde{h}_c(f) = \widetilde{h}_+(f)$ ($\widetilde{h}_s(f) = \widetilde{h}_\times(f)$) for $\phi_c = 0$ and $A_{+,\times} = 1$.

Detection in FCAS is based on the GLRT statistic, defined as

$$\rho^2_{\mathrm{coh}} = \max_{\Theta} \Gamma^2(\Theta) , \tag{14}$$

$$\Gamma^2(\Theta) = \max_{\Theta_{\mathrm{ext}}} \lambda^{(D)} , \tag{15}$$

where Θ_{ext} and Θ are the sets of so-called extrinsic and intrinsic parameters: $\Theta_{\mathrm{ext}} = (t_c, \{A_k\})$, $k = 1, \ldots, 4$, and $\Theta = (\alpha, \delta, \tau_0, \tau_{1.5})$. Maximization over A_k can be carried out analytically while t_c can be efficiently maximized over using the Fast Fourier Transform (FFT). Maximization over Θ must be done numerically and this dominates the overall computational cost of the FCAS. We call $\Gamma^2(\Theta)$ the *coherent fitness function* and ρ_{coh} the *coherent search statistic*.

The MLE estimates of Θ and Θ_{ext} are the global maximizers of the log-likelihood function. Since the log-likelihood differs from $\lambda^{(D)}$ only by a constant for given data, the MLE estimates are obtained for free as part of the GLRT statistic calculation.

D. Efficient evaluation of the log-likelihood ratio

After analytical maximization over A_k in Eq. (15), one is left with the evaluation of $\langle h_k^i(t - \Delta^i) | h_j^i(t - \Delta^i) \rangle$ and $\langle x^i | h_k^i(t - \Delta^i) \rangle$. Each such inner product [cf. Eq. (12)] is implemented using the FFT and involves the element-wise product of two arrays followed by summation, leading to $O(N)$ floating point operations for data segments containing N samples. Substantial savings in the number of floating point operations can, therefore, be obtained by incorporating the following straightforward optimizations in the numerical evaluation of these inner products.

First, the inner product $\langle h_k^i(t - \Delta^i) | h_j^i(t - \Delta^i) \rangle$ is independent of Δ^i since it appears in the phases of the Fourier transforms of both $h_k^i(t - \Delta^i)$ and $h_j^i(t - \Delta^i)$ and cancels out when one is multiplied with the complex conjugate of the other. Since h_k^i depends on just two orthogonal functions, h_c and h_s, ($\langle h_c, h_s \rangle = 0$), $\langle h_k^i, h_j^i \rangle$ depends only on $\langle h_c, h_c \rangle$ and $\langle h_s, h_s \rangle$. These, in turn, do not depend on any of the remaining signal parameters since they all appear in the phase. Thus, $\langle h_c, h_c \rangle$ and $\langle h_s, h_s \rangle$ can be precomputed and stored. Evaluation of $\langle h_k^i(t - \Delta^i) | h_j^i(t - \Delta^i) \rangle$ for given α and δ then simply involves taking algebraic combinations of these stored scalars.

Next, transferring the detector dependent time shift Δ^i in $\langle x^i | h_k^i(t - \Delta^i) \rangle$ to the detector data,

$$\langle x^i | h_k^i(t - \Delta^i) \rangle^i = \langle x^i(t + \Delta^i) | h_k^i(t) \rangle^i . \tag{16}$$

replaces the cost of generating $2D$ waveforms, namely, $h_c(t - \Delta^i)$ and $h_s(t - \Delta^i)$ for $i \leq D$, with that of doing D time shifts.

Finally, we replace the data by over-whitened data, i.e., $\widetilde{x}^i(f) \to \widetilde{x}^i(f)/S_n^i(f)$, at the start of analysis. This saves the cost of division by $S_n^i(f)$ in constructing the integrand of the inner product in Eq. (12) between data and templates.

III. PARTICLE SWARM OPTIMIZATION

The maximization over the intrinsic parameters in Eq. (14), namely $(\alpha, \delta, \tau_0, \tau_{1.5})$, is carried out in `BINARIES` using PSO. By now the technical details of the PSO algorithm are well described in several papers (e.g., NMW), making the brief summary given below adequate for our purpose.

All PSO variants use the basic idea of evaluating the function to be maximized, called the fitness function, at multiple locations, called particles, within a (bounded) search space. The particles move stochastically in the search space following rules, called dynamical equations, that implement a simple model of flocking behavior observed in bird swarms. In this model, the displacement (called velocity in PSO) of each particle from one iteration to the next is affected by two forces, called social and

cognitive, that attract the particle towards the best location found by its neighbors and the best location found by the particle in its history. The iterations are initialized with random locations and velocities. While a variety of termination conditions are available in the literature [19], we use the simplest one where the algorithm is stopped after a specified number, $N_{\rm iter}$ of iterations.

In this paper, we use the same PSO variant, called local best (lbest) PSO [18], that was used for FCAS in NMW. In this variant, neighborhoods of particles are determined by the ring topology: particle indices are arranged on a ring and a specified number of these on either side of a given index identify the neighbors of the corresponding particle. Specifically, the total number of particles is set at 40 with two neighbors for each particle. In contrast, the variant used in WM was global best (gbest) PSO where each particle has all other particles as its neighbors. For the same number of particles, the performance of lbest PSO as configured above has been demonstrated to be better for the FCAS search than gbest PSO.

In common with most practical stochastic optimization methods, PSO is not guaranteed, even asymptotically, to converge to the global maximum. As such, for a finite number of iterations, one can only demand an acceptable probability of convergence to a specified region containing the global maximum. One of the key elements behind the success of PSO in FCAS is the best-of-M-runs strategy [20, 30] for boosting the convergence probability: multiple runs of PSO, utilizing independent random number streams, are performed on the same GW data and the run that terminates with the best (maximum) value of $\Gamma^2(\Theta)$ provides both the coherent search statistic as well as the estimates of Θ and $\Theta_{\rm ext}$.

Along with $N_{\rm iter}$, the number of runs, $N_{\rm runs}$, forms the only set of PSO parameters that are tuned in `BINARIES`. The metric used for tuning these parameters is based on the fact [21] that the global maximum of the coherent fitness function should always be shifted away from the location, Θ_0, of the true signal parameters. This, after all, is what leads to parameter estimation errors in the presence of noise. Consequently, the value of the coherent search statistic found by PSO, denoted as $\rho'_{\rm coh}(N_{\rm runs}, N_{\rm iter})$, should at least be greater than the value, denoted as $\rho^{(0)}_{\rm coh}$, of the coherent fitness function at Θ_0 if convergence to the global maximum is successful. This leads to our definition of the tuning metric:

$$\mathcal{M}\left(N_{\rm runs}, N_{\rm iter}\right) = \Pr\left(\rho'_{\rm coh}(N_{\rm runs}, N_{\rm iter}) < \rho^{(0)}_{\rm coh}\right), \quad (17)$$

where $\Pr(A)$ is the probability of an event A. The goal of tuning is to bring $\mathcal{M}\left(N_{\rm runs}, N_{\rm iter}\right)$ to an acceptably small value. Needless to say, this metric can only be estimated for simulated data where Θ_0 is known.

IV. RUNTIME ANALYSIS

`BINARIES` is implemented in the C programming language and uses the `Intel MKL` multi-threaded numerical algorithms library for computing FFTs. Three nested parallelization layers are implemented. The outer layer uses `LAUNCHER` [31] to distribute independent runs of PSO across different nodes of a distributed computing cluster. In the inner layer, a specified number of `OpenMP` [32] parallel processes (threads) evaluate PSO particle fitness values. Each process is further assigned a specified number of threads for use by `MKL` functions.

We have tested and compared the performance of `BINARIES` on two different computing clusters, namely, Stampede 2 (S2) and Lonestar 5 (LS5) housed in the Texas Advanced Computing Center. The nodes used on S2 have one Intel Xeon Phi Knights Landing (KNL) processor per node with 68 cores supporting up to 4 threads per core. The LS5 nodes used have two Intel Xeon E-5-2690 (Haswell) processors per node with 12 cores each supporting up to 2 threads per core.While these processors also differ in other details such as the clock rate and cache memory size that are pertinent to computational speed, the main determinant for `BINARIES` is the number of concurrent `OpenMP` and `MKL` threads that can be supported. The threads related to fitness evaluations are distributed on all the processing cores of a node, with each node executing one PSO run.

The search space for PSO is typically taken to be a hypercube. Given that the search over the sky in `BINARIES` is not partitioned, this translates into a rectangle in τ_0, $\tau_{1.5}$ space. To cover the entire range of τ_0 and $\tau_{1.5}$ values for CBC signals, a set of rectangles in this space along with their overlap fraction must be prescribed. Since the search in each rectangle can be conducted in parallel, and since the runtime – defined as the wall-clock time taken to complete the analysis of a given segment of data – does not depend on the size of the rectangle searched but on the number of detectors, data duration, number of PSO particles, and the number of PSO iterations, having multiple rectangles does not increase the overall runtime of the PSO-based FCAS search. Similarly, the best-of-M-runs (c.f., Sec. III) strategy does not add to the runtime of `BINARIES` if all the runs are computed in parallel. Thus, for an analysis of runtime, it is sufficient to consider the search over only one rectangular region and one PSO run.

There are two factors that contribute to the computational speed of `BINARIES`: the improved numerical implementation of the mathematical formalism described in Sec. II D and, as described above, the number of parallel `OpenMP` and `MKL` threads used. We fix the number of `OpenMP` threads at 40, the number of PSO particles used in `BINARIES`, while the number of `MKL` threads is varied to find the optimum operating point.

To quantify the effect of the improved numerical implementation and the use of `MKL` threads, we ran `BINARIES` on the same platform (LS5) as the codes used in NMW

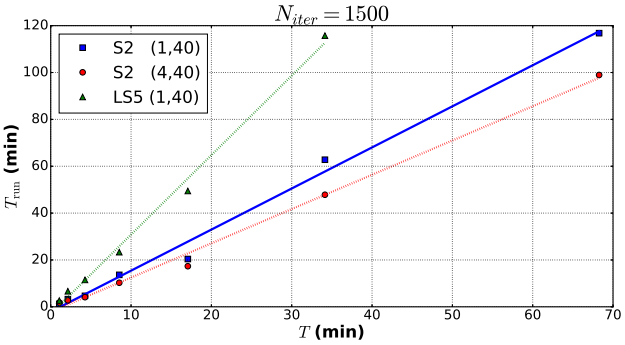


FIG. 2. Runtime, ($T_{\rm run}$), as a function of the duration of data (T) for `BINARIES` running on S2 and LS5 with different numbers of `MKL` threads. The number of `MKL` and `OpenMP` threads are shown as the first and second numbers, respectively, in the parentheses next to the name of the cluster (S2 or LS5). The dependence of $T_{\rm run}$ on T is approximately linear with slope 1.75, 1.46, and 3.39 for S2(1,40), S2(4,40), and LS5(1,40), respectively. For large T, S2 is ≈ 2.3 times faster than LS5. $T_{\rm run}$ in all the cases above is obtained for the number of PSO iterations set to $N_{\rm iter} = 1500$.

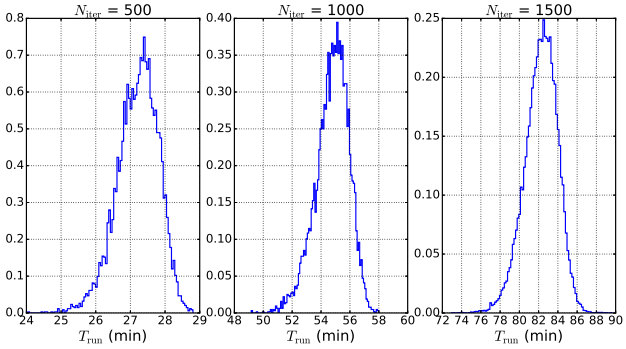


FIG. 3. The distribution of runtime, $T_{\rm run}$, of `BINARIES` on the KNL processor as a function of the number, $N_{\rm iter}$, of PSO iterations for duration of data $T = 60$ min. The 1st, 50th, and 99th percentiles of the runtime (in minutes) are $\{25.6, 27.3, 28.4\}$, $\{51.6, 54.9, 57.0\}$, and $\{77.7, 82.3, 85.7\}$ for $N_{\rm iter} = 500$, 1000, and 1500, respectively. `BINARIES` was run with 40 `OpenMP` and 4 `MKL` threads in all cases. Starting from the lowest $N_{\rm iter}$, the first two histograms were obtained from 7200 trials while the third used 35200 trials.

and found it to be ≈ 22 times faster on average. The effect of different processors, and the different number of threads that they can support, is shown in Fig. 2 where the runtime ($T_{\rm run}$) of `BINARIES` is analyzed across S2 and LS5 as a function of the duration of data (T) and different numbers of `MKL` threads. While, interestingly, the optimum number of `MKL` threads was found to depend on T for short data durations, its best value is 4 for the large T of 60 min considered in this paper. Overall, the change in processor from Haswell to KNL (with 4 `MKL` threads) provides a factor of ≈ 2.3 speed up.

Figure 3 shows the distribution of $T_{\rm run}$ on KNL and its dependence on the number, $N_{\rm iter}$, of PSO iterations for $T = 60$ min. We see that the runtime is quite stable, with a fairly narrow spread, and the average $T_{\rm run}$ has a linear dependence on $N_{\rm iter}$. `BINARIES` attains faster than real time processing speed, $T_{\rm run} < T$, for $N_{\rm iter} \leq 1000$.

Besides the type of processor, the demands a code puts on other hardware parameters must also be noted. Among these, the principal one is the available system random access memory (RAM). The RAM consumed depends on the sampling rate of the data, the use of single (4 bytes) or double (8 bytes) precision data types, length of the data to be analyzed, number of detectors, and most importantly, the number of concurrent PSO particle evaluations. For analysis in double precision of 60 min data sampled at 2048 Hz, `BINARIES` requires a base amount of 576 MB plus 192 MB per detector for evaluating the fitness of a single PSO particle. For a total load of 40 PSO particles, with concurrent evaluation of all fitness values, the RAM required is ≈ 54 GB for a four detector network. For short data stretches of 60 sec, keeping all other variables fixed, the RAM needed is ≈ 900 MB.

V. RESULTS

The performance of `BINARIES` is characterized using simulated data realizations. Each realization consists of 60 min long time series from the four-detector HLVK network at a sampling frequency of 2048 Hz. The noise realizations in each time series are generated following the model described in Sec. II. To have a large number of noise realizations and yet remain within the cycle lengths of standard pesudo-random number generators, we adopt the standard approach used in GW searches for measuring background rates: unphysical and independent time shifts of ≥ 10 sec are applied to the noise time series from the different detectors to generate effectively new noise realizations. For our choice of the time shift and the number of time shifts, 1000 new realizations can be generated from a given data realization in this manner.

We use two different sky locations for generating strain responses: (L4) $\alpha = 32.09°$, $\delta = -53.86°$, and (L5) $\alpha = 150.11°$, $\delta = -60.16°$. The polarization angle is set to be $\psi = 30°$ at both locations. L4 and L5 are two out of the 6 locations used in WM and correspond to the best and worst condition numbers for the antenna pattern matrix $\mathbf{F}(\alpha, \delta, \psi)$ of the HLVK network.

The binary component masses are kept equal and set to 1.5 $M_\odot$. The signal time of arrival at the ECEF origin is set to be 20 min after the start of the data and, for the chosen mass parameters and f_*, the strain response in each detector lasts 15.1 min.

The signals are normalized to have a prescribed network signal to noise ratio (SNR) defined as

$$\text{SNR} = \left[\sum_{i=1}^{D} \langle h^i | h^i \rangle^i\right]^{1/2}, \tag{18}$$

For each location, we generate strain responses with

SNR = 9, 10, 12, and 15.

Results related to H_0 (noise-only) data are obtained from 1000 realizations while 250 H_1 (signal plus noise) data realizations are used for each combination of location and SNR. For the search space of PSO, α and δ cover the entire sky, while $\tau_0 \in [500, 1500]$ sec and $\tau_{1.5} \in [5, 15]$ sec.

In the remainder of this section, we first present the results for PSO tuning followed by the detection and estimation performance of `BINARIES`.

A. PSO tuning

The tuning procedure for PSO involves estimating the metric $\mathcal{M}(N_{\rm runs}, N_{\rm iter})$ defined in Eq. (17) from a set of simulated H_1 data realizations for a given combination of $N_{\rm iter} \in \{500, 1000, 1500\}$, $N_{\rm runs} \in \{4, 8, 12\}$, and SNR. To reduce the computational burden involved in tuning, the number of H_1 data realizations is lowered to 120 and only the L4 location is used.

Figure 4 illustrates how the performance of PSO evolves for a given SNR as $N_{\rm iter}$ and $N_{\rm runs}$ are changed. Given a scatterplot from this figure corresponding to some $N_{\rm iter}$ and $N_{\rm runs}$ combination, the simplest estimate of $\mathcal{M}(N_{\rm runs}, N_{\rm iter})$ is just the fraction of points that fall below the diagonal. This raw estimate can be improved upon using the bootstrap [33] based procedure introduced in NMW.

Table I presents statistical summaries of the sample distribution of $\mathcal{M}(N_{\rm runs}, N_{\rm iter})$ for different combinations of $N_{\rm iter}$, $N_{\rm runs}$, and SNR. We see that the tuning metric moves towards lower values, as desired, with an increase in $N_{\rm iter}$ or $N_{\rm runs}$. Given the number of nodes and the number of threads per node in a distributed computing environment, the table entries can be used to find the appropriate values for $N_{\rm iter}$ and $N_{\rm runs}$ to use. Similarly, given a desired value of the metric, the table allows us to scope out the computing resources needed to achieve that value.

Since the computing clusters available to us could easily accommodate the largest value of $N_{\rm runs}$ in Table I, we simply choose $N_{\rm runs} = 12$ and look for the largest $N_{\rm iter}$ needed to achieve a sufficiently low value of $\mathcal{M}(N_{\rm runs}, N_{\rm iter})$. Following this approach, we see that setting $N_{\rm iter} = 500$ for SNR ≥ 12 already gives a low value of ≤ 0.1 for the first and ≈ 0.1 for the 99th percentile, respectively, of the tuning metric distribution. Thus, we do not need to move further down the table in this case. For SNR ≤ 10, on the other hand, one needs $N_{\rm iter} = 1500$ to meet similar conditions. Thus, in summary, we choose $N_{\rm runs} = 12$, $N_{\rm iter} = 500$, and $N_{\rm runs} = 12$, $N_{\rm iter} = 1500$ for the analysis of data containing SNR ≥ 12 and SNR ≤ 10 signals, respectively.

When analyzing real data, one would need to fix a target minimum SNR at which good performance of PSO is required and proceed in the same manner as above to tune $N_{\rm runs}$ and $N_{\rm iter}$. The training data for tuning in this case could either be simulated or derived from a section of real data that is set aside for this purpose. There would be a single set of $N_{\rm iter}$ and $N_{\rm runs}$ values when searching real data and a single detection threshold derived from the analysis of H_0 data with these parameters. However, for simulated data, where the signal SNR is known a priori, we can reduce computational costs by using $N_{\rm iter}$ and $N_{\rm runs}$ tuned to different target minimum SNRs. For example, we can use the values tuned for a target minimum SNR = 12 instead of SNR = 9 to analyze data with SNR = 15 signals since this reduces the computational burden of the simulation without significantly affecting detection performance.

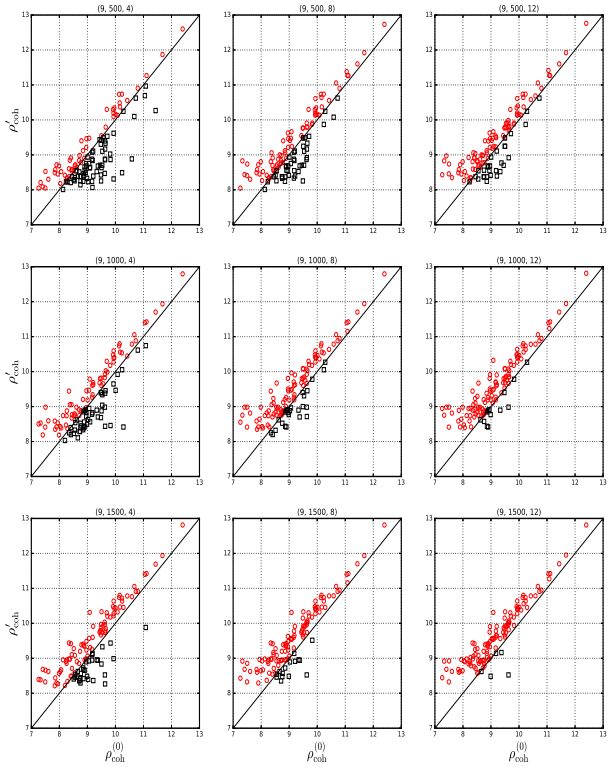


FIG. 4. Scatterplots of the coherent search statistic found by PSO, $\rho'_{\rm coh}(N_{\rm runs}, N_{\rm iter})$, and the coherent fitness value at the true signal parameters, $\rho^{(0)}_{\rm coh}$, for an SNR = 9 source at the L4 location. Each subplot corresponds to the combination of $N_{\rm iter}$ and $N_{\rm runs}$ stated in its title as (SNR,$N_{\rm iter}$,$N_{\rm runs}$), and shows the values of $\rho'_{\rm coh}(N_{\rm runs}, N_{\rm iter})$ and $\rho^{(0)}_{\rm coh}$ for 120 data realizations. Points (black) below the diagonal indicate instances in which PSO failed to converge to the global maximum of the coherent fitness function.

Relating the tuned value of $N_{\rm iter}$ for SNR = 9 to the distribution of runtimes presented in Fig. 3, the runtime of `BINARIES` for four-detector data on a KNL cluster can be expected to take $\approx 40\%$ longer than real-time. If the target minimum SNR is increased to $\gtrsim 12$, for which $N_{\rm iter} = 500$, `BINARIES` can analyze data at almost twice real-time speed with a 60 min data segment processed in ≈ 27 min on the average.

TABLE I. The PSO tuning metric $\mathcal{M}(N_{\rm runs}, N_{\rm iter})$ for a discrete set of SNR values. For each $N_{\rm runs}$ and $N_{\rm iter}$ combination, there are four rows corresponding (from top to bottom) to SNR = 9, 10, 12 and 15, respectively. In each row, the numbers from left to right are the 1st and the 99th percentiles of the sample distribution of $\mathcal{M}(N_{\rm runs}, N_{\rm iter})$, respectively.

$N_{\rm iter}$	$N_{\rm runs}=2$		$N_{\rm runs}=4$		$N_{\rm runs}=6$		$N_{\rm runs}=8$		$N_{\rm runs}=10$		$N_{\rm runs}=12$	
500	0.633	0.783	0.517	0.667	0.433	0.583	0.383	0.525	0.342	0.483	0.317	0.450
	0.633	0.792	0.483	0.650	0.408	0.558	0.358	0.500	0.325	0.450	0.300	0.417
	0.325	0.500	0.183	0.325	0.125	0.242	0.092	0.192	0.075	0.167	0.067	0.142
	0.042	0.150	0	0.058	0	0.033	0	0.025	0	0.017	0	0.017
1000	0.450	0.608	0.308	0.467	0.233	0.375	0.192	0.317	0.167	0.275	0.142	0.250
	0.425	0.583	0.292	0.433	0.233	0.358	0.200	0.317	0.183	0.283	0.167	0.258
	0.100	0.217	0.033	0.117	0.017	0.083	0.008	0.067	0.008	0.058	0.008	0.050
	0	0.033	0	0.008	0	0.008	0	0	0	0	0	0
1500	0.333	0.492	0.192	0.333	0.133	0.250	0.092	0.208	0.075	0.175	0.058	0.150
	0.308	0.467	0.192	0.317	0.133	0.250	0.108	0.208	0.092	0.183	0.083	0.167
	0.042	0.133	0.008	0.067	0.008	0.042	0.008	0.033	0.008	0.025	0.008	0.025
	0	0.017	0	0	0	0	0	0	0	0	0	0

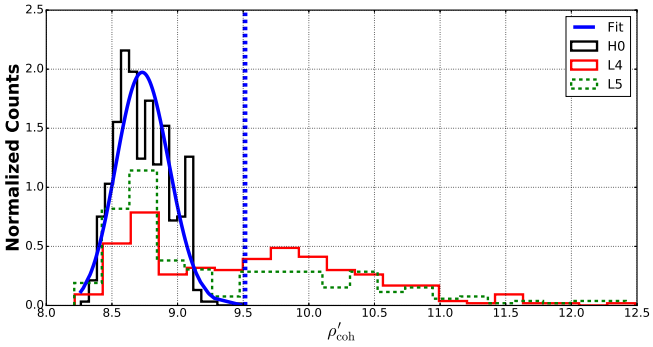


FIG. 5. Histograms of the coherent search statistic found by PSO, $\rho'_{\rm coh}(12, 1500)$, under the (black curve) H_0 and (red and green curves) H_1 hypotheses for SNR = 9. Under H_1, the histograms corresponding to the source locations (red) L4 and (green) L5 are shown separately. Also shown (solid blue curve) is the best-fit lognormal probability density function for the H_0 distribution. The dashed line at $\rho'_{\rm coh} = 9.5$ marks the detection threshold obtained from the best-fit for a false alarm rate of 1 event per year. The p-value of the two-sample KS test between the H_1 samples is 7.2×10^{-5}. Retaining only $\rho'_{\rm coh} > 9.0$ results in a p-value of 0.33.

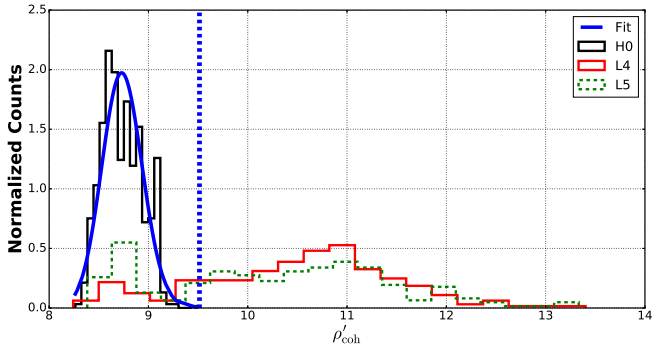


FIG. 6. Same as Fig. 5 except that SNR = 10 and the p-value of the two-sample KS test is 0.02. Retaining only $\rho'_{\rm coh} > 9.0$ results in a p-value of 0.83.

B. Detection performance

Figures 5 to 8 show the estimated distributions of the coherent search statistic found by PSO, $\rho'_{\rm coh}$, under the H_0 and H_1 hypotheses for different SNR values. The H_0 distributions in each figure are obtained using the values of $N_{\rm iter}$ and $N_{\rm runs}$ tuned, as described above, for the respective SNR. The distribution under H_1 is shown separately for the two source locations, L4 and L5.

A comparison of the H_1 histograms at a given SNR shows that the distribution of the coherent search statistic is principally governed by SNR. However, the condition number of the antenna pattern matrix, $\mathbf{F}(\alpha, \delta, \psi)$, at the source location also has an effect. This is indicated by performing a two-sample Kolmogorov-Smirnov (KS) test of the null hypotheses that the two H_1 sam-

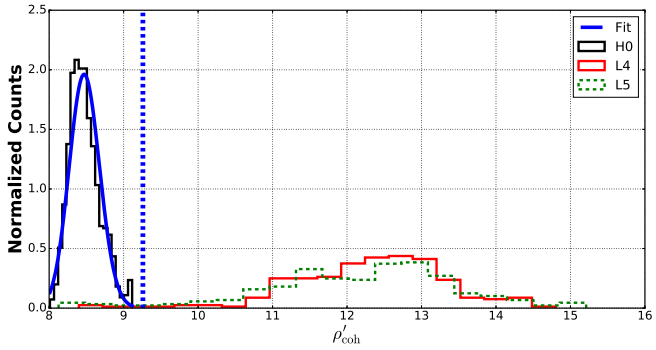


FIG. 7. Histograms of the coherent search statistic found by PSO, $\rho'_{\rm coh}(12, 500)$, under the (black curve) H_0 and (red and green curves) H_1 hypotheses for SNR = 12. Under H_1, the histograms corresponding to the source locations (red) L4 and (green) L5 are shown separately. Also shown (solid blue curve) is the best-fit lognormal probability density function for the H_0 distribution. The dashed line at $\rho'_{\rm coh} = 9.3$ marks the detection threshold obtained from the best-fit for a false alarm rate of 1 event per year. The p-value of the two-sample KS test between the H_1 samples is 0.23. Retaining only $\rho'_{\rm coh} > 9.0$ results in a p-value of 0.48.

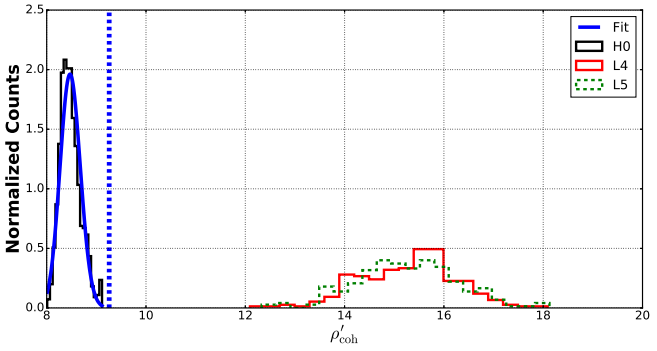


FIG. 8. Same as Fig. 7 except that SNR = 15 and the p-value of the two-sample KS test is 0.52. There is no change in the p-value when retaining only $\rho'_{\rm coh} > 9.0$ because all the values satisfy this cutoff.

ples are drawn from the same probability distribution. The p-value of the test – the probability of obtaining the observed KS statistic value under the null hypothesis – is listed in the captions of the figures. It suggests a clear difference between the probability distributions at SNR ≤ 10 but a statistically insignificant difference for SNR $\gtrsim 12$. It is interesting to note that for the shorter data length (64 sec) used in NMW, the two distributions did not differ significantly even for SNR = 9.

The two-sample KS test was also carried out between the H_1 samples after excluding values of $\rho'_{\rm coh} < 9.0$. Under this restriction, the p-value in all cases indicates that there is no statistically significant difference between the two samples. All of the difference clearly arises from the distribution of $\rho'_{\rm coh}$ at low values. Since the cut-off value of 9.0 is below any reasonable detection threshold (see below), this implies that the distribution of $\rho'_{\rm coh}$ values for detected signals will always be observed to be independent of GW source location (for at least SNR ≥ 9.0 tested here).

The distribution of $\rho'_{\rm coh}$ under H_0 is observed to change for different values of $N_{\rm iter}$, with a shift towards lower values for smaller $N_{\rm iter}$. This can be understood qualitatively from the fact that, unlike the case of H_1, the fitness function under H_0 has many local maxima dispersed throughout the search space with comparable heights. The likelihood of PSO missing the global maximum is, therefore, higher in this case as its exploration ability, which is controlled by $N_{\rm iter}$, is reduced. Consequently, lower $\rho'_{\rm coh}$ values are found by PSO under H_0 for lower $N_{\rm iter}$. This effect is quite mild, however, leading to only a marginal change in the detection threshold.

For a fiducial false alarm rate (FAR) of 1 false event per year, the false alarm probability per 60 min data segment is 1.14×10^{-4} if there is no overlap between consecutive segments. The corresponding detection threshold, obtained by fitting a log-normal distribution to the H_0 histograms, for $N_{\rm iter} = 1500$ and $N_{\rm runs} = 12$, is $\eta = 9.5$. The same procedure for the H_0 histogram under $N_{\rm iter} = 500$ and $N_{\rm runs} = 12$ yields a slightly lower threshold of 9.3.

TABLE II. Detection probabilities for all combinations of SNR and sky locations at a detection threshold of $\eta = 9.5$ corresponding to a FAR of ≈ 1 false event per year. Also listed (third column) is the loss in detection probability, $L_{\rm DP}$, defined in Eq. (19). The last two columns separate the contributions to $L_{\rm DP}$ by the two sky locations used for generating data realizations.

SNR	L4	L5	$L_{\rm DP}$	$L_{\rm DP}$/L4	$L_{\rm DP}$/L5
9	0.504	0.372	11.798%	0.000%	21.429%
10	0.820	0.720	4.324%	0.538%	8.152%
12	0.992	0.972	1.613%	0.806%	2.419%
15	1.0	1.0	0.000%	0.000%	0.000%

Table II shows detection probabilities for different combinations of SNR and sky locations under the conservative choice of using the higher detection threshold. The effect of antenna pattern condition number is clear: for low SNR values, the detection probability at L5 is markedly worse than at L4. The effect of the condition number and, consequently, the discrepancy in detection probability dissipates for SNR $\gtrsim 12$.

The necessarily finite and typically small sample size used for tuning PSO means that the true value of the metric $\mathcal{M}\left(N_{\rm runs}, N_{\rm iter}\right)$ need not be zero even when its estimated value from the sample is. For a sufficiently large number of trials, therefore, there will always be a finite fraction in which the coherent search statistic value found by PSO, $\rho'_{\rm coh}$, drops below the coherent fitness at the true location, $\rho^{(0)}_{\rm coh}$. However, while each such dropout is an instance of failure to converge to the global maximum of the coherent fitness function, what matters is the loss in the detection probability that this entails. Detection probability is reduced by a dropout event only if $\rho^{(0)}_{\rm coh}$ exceeds the detection threshold but $\rho'_{\rm coh}$ does not. To measure this effect, we define the loss in detection probability,

$$L_{\rm DP} = P(\rho'_{\rm coh} \leq \eta | \rho^{(0)}_{\rm coh} \geq \eta) \,, \tag{19}$$

where $P(A|B)$ denotes the conditional probability of event A given event B, and η is the detection threshold. An examination of the estimated $L_{\rm DP}$ values shown in Table II shows that it decreases quite rapidly as SNR increases, becoming too small to measure with our simulations for SNR = 15. As with the detection probability, we have also shown $L_{\rm DP}$ for each location separately, and it is evident that again the condition number has a major effect with L5 showing a significantly higher loss in detection probability. In fact, the loss in detection probability at SNR = 9 arises entirely from the L5 data realizations.

A feature of the distribution of the coherent search statistic under H_1 that may appear surprising at first is the appearance of a bump, seen as an excess in histogram counts, at low values. This excess is reduced (see Fig. 6) and ultimately disappears (cf. Figures 7 and 8) as the signal SNR goes up. The appearance of this bump is simply due to the coherent search statistic being the global

maximum of the coherent fitness function, not its value at a fixed location. The presence of a signal only affects the distribution of coherent fitness function values in a small region of the full parameter space, the distribution elsewhere being close to that for H_0 data. For a sufficiently weak signal, the probability that the global maximum escapes from the small region affected by the signal is higher. When this happens, the value of the coherent search statistic is drawn from its distribution under H_0. For a strong signal, on the other hand, the global maximum stays confined to the region close to the signal and its governing distribution is that under H_1. In other words, the distribution of the coherent search statistic in the presence of a signal is actually a mixture of two distributions with the probability of sampling from either depending on the strength of the signal. A counterpart of this effect is also seen in Fig. 4, where a leveling off is observed in the values of $\rho'_{\rm coh}$ at low values of $\rho^{(0)}_{\rm coh}$.

C. Estimation performance

The parameter estimation performance of `BINARIES` is characterized here for SNR $\in \{12, 15\}$ for which the corresponding detection probabilities (cf. Table II) are near unity. Figures 9 and 10 show the distribution of the estimated sky locations at these SNR values. They follow the same pattern as seen in NMW for shorter signals: while the estimated locations of a source at L4 are fairly well-clustered around the true value, two distinct clusters appear for a source at L5. The secondary cluster of estimated locations in the latter case appears close to the point that is antipodal to the true location. This is a clear manifestation of the condition number of the antenna pattern matrix $\mathbf{F}(\alpha, \delta, \psi)$, which is worse at L5 than L4, and consistent with its effect on detection probabilities at lower SNR values. While its deleterious effect on detection probability disappears for SNR $\in \{12, 15\}$, it remains in force for sky localization error.

It is important to emphasize here that, as was determined during the tuning process, PSO almost always converges to the global maximum for SNR $\in \{12, 15\}$. This indicates strongly that the appearance of the secondary cluster of locations is not due to a failure in convergence to the global maximum but its actual jump to that location due to the effect of noise. The exact mechanism by which the condition number creates a secondary location is yet to be elucidated and is left to future work.

Figures 11 and 12 show the distribution of estimated chirp time parameters corresponding to sources at L4 and L5. The condition number of the antenna pattern matrix does not have any noticeable effect on these distributions. This is consistent with the known result, from CRLB analysis, that errors in sky location have low correlation with errors in the chirp times [15].

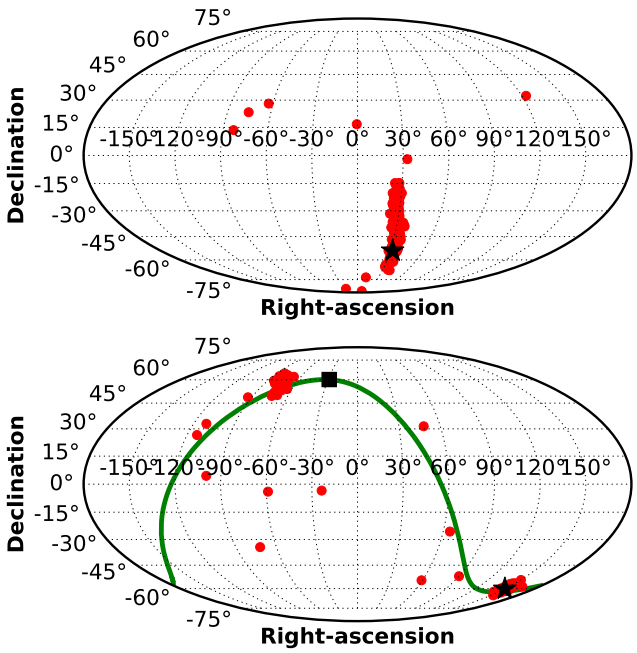


FIG. 9. Estimated sky location of a SNR = 12 source at (top) L4 and (bottom) L5 locations. In both plots the true location of the source is shown by a star, and estimated locations from H_1 data realizations are shown by red circles. In the bottom plot, the square shows the antipode of the true location.

VI. DISCUSSION

We have presented performance results for a new code, called `BINARIES`, that implements a PSO-based FCAS search. Using this code we were able to verify that the PSO-based search, which had previously been demonstrated for few minute long data segments in WM [22] and NMW [23], can be extended to the analysis of the longest data length needed for CBC searches.

The `BINARIES` code differs significantly from the code used previously in NMW: (i) A new and more efficient numerical implementation of the mathematical formalism underlying FCAS search is used, and (ii) a third parallelization layer is introduced using a multi-threaded numerical algorithms library. Together, these changes result in a factor of ≈ 22 enhancement in the speed of the code.

Simulated 60 min long data realizations from a network of four second-generation detectors (HLVK) at their respective design sensitivities were generated for different source locations and SNR values. The mass parameters of the source were chosen to be $(1.5, 1.5)\ M_\odot$, which is representative of long duration CBC signals. Depending on the target minimum SNR, the runtime of `BINARIES` ranges from 40% slower than real time to about twice as fast. For the latter, it is possible to detect SNR $\gtrsim 12$ signals with a detection probability of nearly unity at a FAR of ≈ 1 false event per year. This is the first demonstration that the computational barrier confronting an always-on

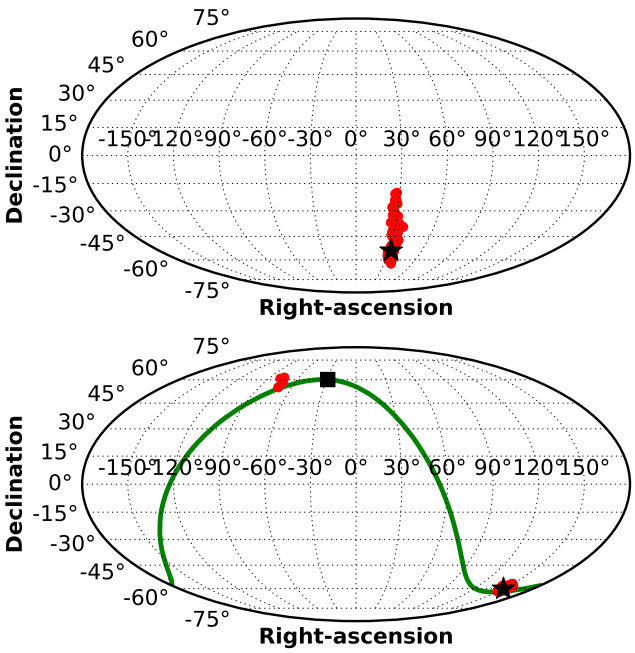


FIG. 10. Same as Fig. 9 but for SNR=15.

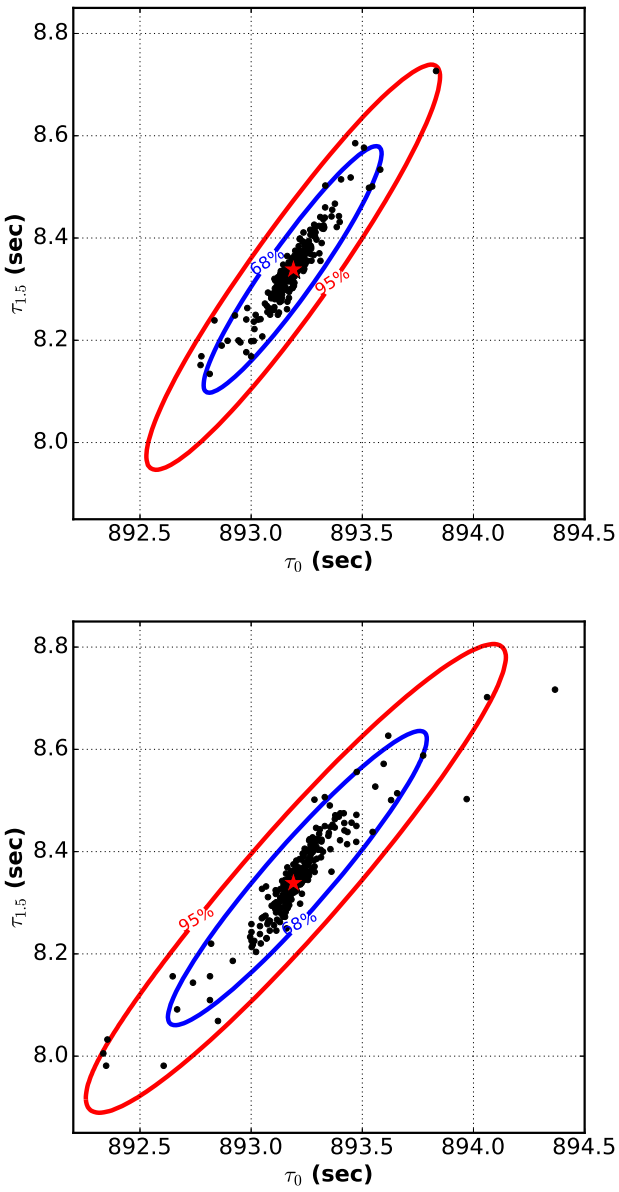


FIG. 11. Estimated chirp times for a SNR = 12 source at (top) L4 and (bottom) L5 locations. In both plots the true values of the chirp times are marked by a star, and estimated values from H_1 data realizations are shown by black dots. The contours shown include (blue) 68% and (red) 95% of the total probability of a kernel density estimate, obtained using a Gaussian kernel with a bandwidth of 2, of the 2-dimensional probability density function.

FCAS search, which promises substantially better sensitivity than semi-coherent searches, is not insurmountable at astrophysically relevant signal strengths.

Analysis of H_0 (noise-only) data shows that SNR = 9 falls below the detection threshold required by the FAR chosen in this paper. This could be an intrinsic feature of a four detector network or the result of PSO failing to converge often enough to the global maximum of the coherent fitness function. For the current choice of PSO variant, a realistic signal strength that allows confident detections is SNR ≈ 10 for which the detection probability is $\gtrsim 70\%$.

It should be emphasized here that the network SNR values above correspond to a four-detector network. In the simple case where a signal has equal single-detector SNR across a network, an SNR = 10 corresponds to a two-detector SNR = $(10/\sqrt{4}) \times \sqrt{2} = 7.07$, which is below the network SNR of events reported in current LIGO-only semi-coherent searches. Moreover, the detection probability for a given SNR and number of detectors also depends on the mass range of the search. In NMW, where a high mass binary with a total mass of 29 $M_\odot$ was used as an example, a detection probability of $\approx 70\%$, at a false alarm rate of 1 false event per year, was achieved for a lower four-detector SNR = 9.

Our study of sky localization error highlights the important effect of the condition number of the antenna pattern matrix, which measures the ill-posedness of the GW network analysis problem arising from the relative orientations of detectors. It was found that the error region on the sky can split into two widely separated areas for a source location having a high condition number. The detection probability for such a source is also reduced although this is a significant effect only for SNR $\lesssim 10$. The loss in detection probability, caused by the failure of PSO to converge to the global maximum, is consistently higher for the source location having a higher condition number. The above results suggest that incorporating some form of regularization [34–36] in the derivation of the coherent search statistic for CBC signals is important for improving sky localization and detection sensitivity.

The number of parallelization layers used in `BINARIES`

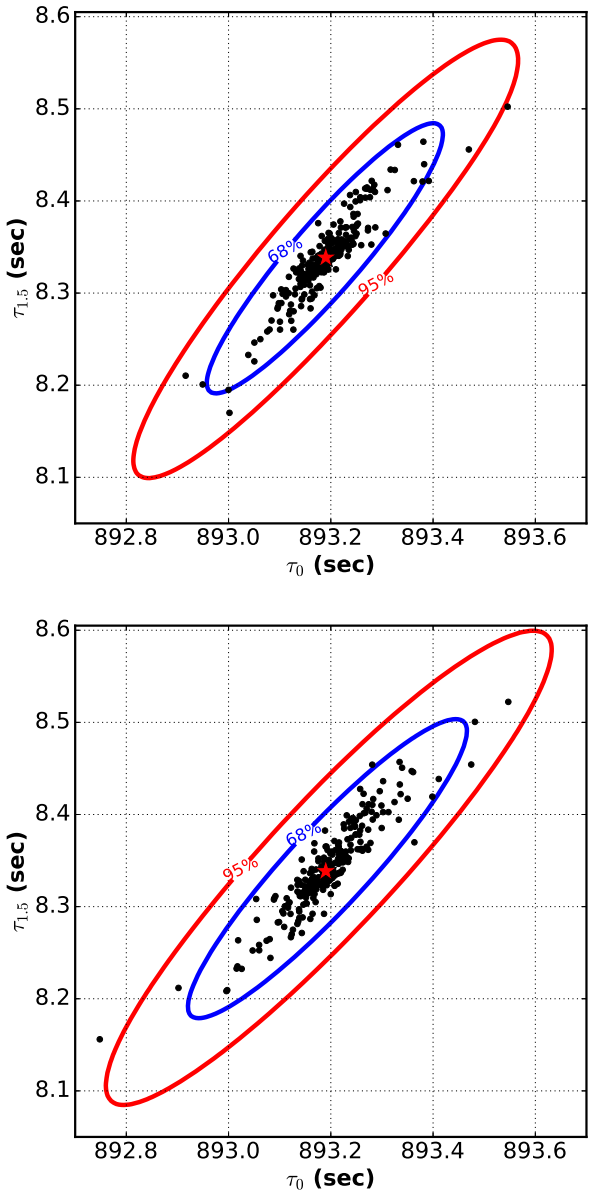


FIG. 12. Same as Fig. 11 except SNR = 15.

can be increased by offloading the bulk of the computations involved in fitness evaluation, such as the inner product of arrays in Eq. (16), to Graphics Processing Units (GPUs). Given that a larger number of MKL threads leads to a significantly faster processing speed, the $O(10^3)$ threads available on GPUs promise to provide an even greater improvement. This investigation is currently in progress.

While `BINARIES` has been applied to simulated data in this paper, our eventual goal is to apply it to O1, O2, and future open data. This requires embedding `BINARIES` in an end-to-end search pipeline that includes data conditioning, glitch vetoes, post-processing, and background rate analysis. Results from the analysis of real data following the completion of the full pipeline will be reported in future papers.

ACKNOWLEDGEMENTS

The contribution of S.D.M. to this paper was supported by National Science Foundation (NSF) grant PHY-1505861. We acknowledge the Texas Advanced Computing Center (TACC) at The University of Texas at Austin for providing HPC resources that have contributed to the research results reported within this paper. URL: www.tacc.utexas.edu.

[1] B. P. Abbott *et al.*, "Observation of gravitational waves from a binary black hole merger," *Physical Review Letters*, vol. 116, p. 061102, Feb 2016.

[2] P. Fritschel, "Second generation instruments for the Laser Interferometer Gravitational Wave Observatory (LIGO)," in *Gravitational-Wave Detection* (M. Cruise and P. Saulson, eds.), vol. 4856 of *Society of Photo-Optical Instrumentation Engineers (SPIE) Conference Series*, pp. 282–291, Mar. 2003.

[3] B. Abbott, R. Abbott, T. Abbott, S. Abraham, F. Acernese, K. Ackley, C. Adams, R. Adhikari, V. Adya, C. Affeldt, *et al.*, "Gwtc-1: A gravitational-wave transient catalog of compact binary mergers observed by ligo and virgo during the first and second observing runs," *Physical Review X*, vol. 9, no. 3, p. 031040, 2019.

[4] J. Degallaix, T. Accadia, F. Acernese, M. Agathos, A. Allocca, *et al.*, "Advanced Virgo Status," in *9th LISA Symposium* (G. Auger, P. Binétruy, and E. Plagnol, eds.), vol. 467 of *Astronomical Society of the Pacific Conference Series*, p. 151, Jan. 2013.

[5] B. P. Abbott *et al.*, "GW170817: Observation of gravitational waves from a binary neutron star inspiral," *Physical Review Letters*, vol. 119, p. 161101, Oct 2017.

[6] B. P. Abbott *et al.*, "Multi-messenger observations of a binary neutron star merger," *The Astrophysical Journal Letters*, vol. 848, no. 2, p. L12, 2017.

[7] K. Somiya, "Detector configuration of KAGRA-the Japanese cryogenic gravitational-wave detector," *Classi-*

cal and Quantum Gravity, vol. 29, p. 124007, June 2012.

[8] C. S. Unnikrishnan, "Indigo and ligo-india: Scope and plans for gravitational wave research and precision metrology in india," *International Journal of Modern Physics D*, vol. 22, no. 01, p. 1341010, 2013.

[9] A. Pai, S. Dhurandhar, and S. Bose, "Data-analysis strategy for detecting gravitational-wave signals from inspiraling compact binaries with a network of laser-interferometric detectors," *Physical Review D*, vol. 64, p. 042004, Jul 2001.

[10] S. Kay, *Fundamentals of Statistical Signal Processing, Volume I: Estimation Theory*. Prentice Hall, 1st ed., 1993.

[11] S. Kay, *Fundamentals of Statistical Signal Processing, Volume II: Detection Theory*. Prentice Hall, 1998.

[12] D. Macleod, I. W. Harry, and S. Fairhurst, "Fully-coherent all-sky search for gravitational-waves from compact binary coalescences," *Physical Review D*, vol. 93, p. 064004, Mar 2016.

[13] B. P. Abbott *et al.*, "GW150914: First results from the search for binary black hole coalescence with Advanced LIGO," *Physical Review D*, vol. 93, Jun 2016.

[14] J. Veitch *et al.*, "Parameter estimation for compact binaries with ground-based gravitational-wave observations using the lalinference software library," *Physical Review D*, vol. 91, no. 4, p. 042003, 2015.

[15] L. P. Singer and L. R. Price, "Rapid bayesian position reconstruction for gravitational-wave transients," *Physical Review D*, vol. 93, no. 2, p. 024013, 2016.

[16] S. Chatterji, A. Lazzarini, L. Stein, P. J. Sutton, A. Searle, and M. Tinto, "Coherent network analysis technique for discriminating gravitational-wave bursts from instrumental noise," *Physical Review D*, vol. 74, no. 8, p. 082005, 2006.

[17] J. Kennedy and R. C. Eberhart, "Particle swarm optimization," in *Proceedings of the IEEE International Conference on Neural Networks: Perth, WA, Australia*, vol. 4, p. 1942, IEEE, 1995.

[18] D. Bratton and J. Kennedy, "Defining a standard for particle swarm optimization," in *Swarm Intelligence Symposium, 2007. SIS 2007. IEEE*, pp. 120–127, IEEE, 2007.

[19] A. P. Engelbrecht, *Fundamentals of computational swarm intelligence*, vol. 1. Wiley Chichester, 2005.

[20] S. D. Mohanty, *Swarm Intelligence Methods for Statistical Regression*. Chapman and Hall/CRC, 2018.

[21] Y. Wang and S. D. Mohanty, "Particle swarm optimization and gravitational wave data analysis: Performance on a binary inspiral testbed," *Physical Review D*, vol. 81, p. 063002, 2010.

[22] T. S. Weerathunga and S. D. Mohanty, "Performance of particle swarm optimization on the fully-coherent all-sky search for gravitational waves from compact binary coalescences," *Physical Review D*, vol. 95, no. 12, p. 124030, 2017.

[23] M. E. Normandin, S. D. Mohanty, and T. S. Weerathunga, "Particle swarm optimization based search for gravitational waves from compact binary coalescences: Performance improvements," *Physical Review D*, vol. 98, no. 4, p. 044029, 2018.

[24] V. Srivastava, K. R. Nayak, and S. Bose, "Toward low-latency coincident precessing and coherent aligned-spin gravitational-wave searches of compact binary coalescences with particle swarm optimization," *arXiv preprint arXiv:1811.02401*, 2018.

[25] D. T. Alfred Leick, Lev Rapoport, *GPS Satellite Surveying*. Wiley, 2004.

[26] D. Shoemaker, "Advanced ligo anticipated sensitivity curves," Tech. Rep. T0900288-v3, Laser Interferometer Gravitational Wave Observatory, 2010.

[27] LCGT Special Working Group, "Study report on lcgt interferometer observation band," Tech. Rep. JGW-T1000065-v1, Sep 2009.

[28] Virgo Collaboration, "Advanced virgo baseline design," Tech. Rep. VIR-0027A-09, Aug 2009.

[29] L. Blanchet, T. Damour, B. R. Iyer, C. M. Will, and A. G. Wiseman, "Gravitational-radiation damping of compact binary systems to second post-newtonian order," *Physical Review Letters*, vol. 74, pp. 3515–3518, May 1995.

[30] M. Birattari and M. Dorigo, "How to assess and report the performance of a stochastic algorithm on a benchmark problem: mean or best result on a number of runs?," *Optimization letters*, vol. 1, no. 3, pp. 309–311, 2007.

[31] L. A. Wilson and J. M. Fonner, "Launcher: A shell-based framework for rapid development of parallel parametric studies," in *Proceedings of the 2014 Annual Conference on Extreme Science and Engineering Discovery Environment*, XSEDE '14, (New York, NY, USA), pp. 40:1–40:8, ACM, 2014.

[32] L. Dagum and R. Menon, "Openmp: An industry-standard api for shared-memory programming," *IEEE Comput. Sci. Eng.*, vol. 5, pp. 46–55, Jan. 1998.

[33] B. Efron, "Bootstrap methods: another look at the jackknife," in *Breakthroughs in statistics*, pp. 569–593, Springer, 1992.

[34] S. Klimenko, S. Mohanty, M. Rakhmanov, and G. Mitselmakher, "Constraint likelihood analysis for a network of gravitational wave detectors," *Physical Review D*, vol. 72, p. 122002, Dec. 2005.

[35] S. D. Mohanty, M. Rakhmanov, S. Klimenko, and G. Mitselmakher, "Variability of signal-to-noise ratio and the network analysis of gravitational wave burst signals," *Classical and Quantum Gravity*, vol. 23, pp. 4799–4809, Aug. 2006.

[36] M. Rakhmanov, "Rank deficiency and Tikhonov regularization in the inverse problem for gravitational-wave bursts," *Classical and Quantum Gravity*, vol. 23, p. 673, Oct. 2006.